arXiv:1607.02934v1 [quant-ph] 11 Jul 2016

Measurement-enhanced determination of BEC phase diagrams

Mark G. Bason,[1,2,*] Robert Heck,[1,*] Mario Napolitano,[1] Ottó Elíasson,[1] Romain Müller,[1] Aske Thorsen,[1] Wen-Zhuo Zhang,[1,3] Jan Arlt,[1] and Jacob F. Sherson[1,†]

[1]*Department of Physics and Astronomy, Aarhus University, DK-8000 Aarhus C, Denmark*
[2]*Present address: School of Physics & Astronomy, The University of Nottingham, Nottingham NG7 2RD, UK*
[3]*Present address: Innovation Center of Quantum Information and Quantum Physics, Chinese Academy of Sciences, University of Science and Technology, Shanghai, China.*

(Dated: July 12, 2016)

We demonstrate how dispersive atom number measurements during evaporative cooling can be used for enhanced determination of the non-linear parameter dependence of the transition to a Bose-Einstein condensate (BEC). Our analysis demonstrates that conventional averaging of shot-to-shot fluctuations introduces systematic errors and reduces precision in comparison with our method. We furthermore compare in-situ images from dispersive probing of a BEC with corresponding absorption images in time-of-flight. This allows for the determination of the transition point in a single experimental realization by applying multiple dispersive measurements. Finally, we explore the continuous probing of several consecutive phase transition crossings using the periodic addition of a focused "dimple" potential.

Quantum effects have become increasingly important in the development of modern technologies and have led to the need for accurate quantum simulation [1, 2]. A range of approaches, including cold atoms [3–5] and ions [6], superconducting circuits [7], and photons [8] are used to perform such simulations. In particular, many quantum simulators aim to pin down the boundaries between discrete phases of many-body systems, such as Ising spin transition points [4, 6] or magnetic phases [5], with the highest possible accuracy. Current simulations focus on providing tight experimental bounds for benchmarking theoretical models, such as finite temperature bosonic superfluids in optical lattices [9].

In recent years, dispersive light-matter interaction based Quantum Non-Demolition (QND) measurements have emerged as an important tool for the detection and control of quantum many-body systems. Dispersive probing of Bose-Einstein Condensates (BECs) was realized in pioneering work [10, 11] and has since then been employed to continuously monitor the formation of a BEC following a sudden quench [12] and the appearance and dynamics of solitons [13, 14]. In cold atomic clouds, dispersive measurements have been used to moderately reduce classical number fluctuations [15] and to demonstrate active atom number stabilization to the 10^{-3} level [16]. Quantum noise-limited probing and feedback would enable the line-width reduction of atom lasers [17], the stabilization of BECs against spontaneous emission [18], and to squeeze and entangle Bogoliubov excitations [19]. If extended to optical lattices, it would allow for QND detection of quantum phase transitions [20, 21] as well as Schrödinger cat state generation [22, 23] and arbitrary quantum state engineering using tunneling [22] and pinned [24] atoms. To realize its full potential, however, careful studies of the fundamental information-disturbance trade-off [5, 25, 27–29] associated with dispersive imaging is required.

In this Letter we demonstrate that dispersive probing employed during the evaporation sequence allows for enhanced precision in the determination of quantum phase diagrams–

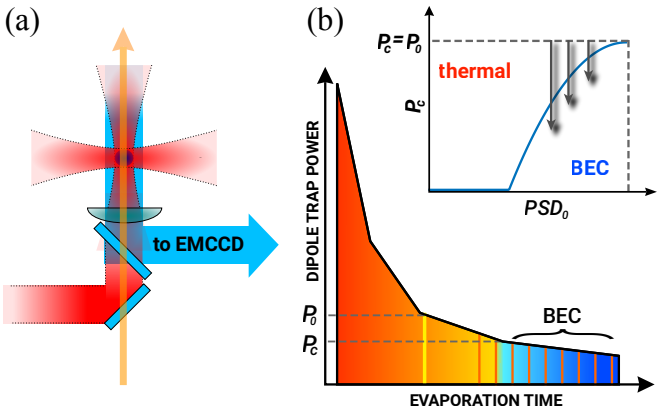

Figure 1. (Color online) (a) Experimental setup showing crossed dipole trap (red) at a wavelength of 1064 nm and the imaging lens. Detuned light (blue) is used to dispersively probe the BEC phase transition. A dimple potential (orange arrow) at a wavelength of 912 nm allows for repeated phase transition crossings. (b) Evaporation scheme illustrating the dispersive "benchmark" pulse at P_o (yellow) and the probing around the phase transition (red) realized either with destructive absorption imaging or with multiple dispersive probe pulses. The inset schematically shows the *critical curve* describing the power, P_c, at which the transition to a BEC occurs, as a function of the dispersively measured phase space density, PSD_o, measured at P_o. The arrows illustrate the paths of individual experimental realizations for different PSD_o.

here, the determination of the critical point in the transition from a thermal cloud to a BEC. First we show that an in-sequence non-destructive measurement of the atom number can be used as a benchmark to bin the subsequently acquired data. This additional information allows for high-resolution mapping of the non-linear parameter dependence despite significant realization-to-realization fluctuations. We furthermore perform a detailed comparison of in-situ images from dispersive probing and equivalent absorption images in time-of-flight. This allows for the single-shot determination of the critical point using multiple dispersive probe pulses as well as

the quantification of the deterministic shift of the phase transition due to probe induced heating. Finally, we probe several consecutive phase transitions using the periodic addition of a focused "dimple" potential in a single experimental realization.

Our experimental setup is shown in Fig. 1(a). Atoms are prepared in the $|\mathrm{F}=2,\mathrm{m_F}=2\rangle$ state of ^{87}Rb and loaded into a crossed dipole trap consisting of two orthogonal, focused 1064 nm laser beams with waists of 70 µm. Forced evaporative cooling is performed by lowering the power in each beam from an initial power 5.5 W to final values between 900 and 600 mW, at which stage partially condensed clouds with condensed fractions $N_0/N \approx 0$–0.6 and total atom numbers $N \approx 2.1$–$0.8 \cdot 10^6$ are produced.

Non-destructive, dispersive measurements of the cloud are recorded using Dark Field Faraday Imaging (DFFI) [5]. In this technique the Faraday effect leads to a rotation of the incoming linear light polarization proportional to the column density of an atomic cloud. To implement this, probing light blue detuned by Δ = 1.5 GHz from the $|\mathrm{F}=2\rangle \rightarrow |\mathrm{F'}=3\rangle$ transition propagates along the same axis as one of the dipole trap beams (z). Intensities of 10 mW/cm^2 are used, corresponding to around 400 photons/(µm^2 µs). A small bias magnetic field of around 1 G along the light propagation direction preserves the atomic sample's spin polarization. By inserting a polarizing beam splitting cube with a suppression factor of $3 \cdot 10^{-4}$ in the imaging path, only the rotated component of the light is imaged onto an Electron Multiplying Charge Coupled Device (EMCCD) camera with an effective resolution of 3–4 µm.

In each realization of the experiment, a 20 µs dispersive benchmark (DB) light pulse probes the thermal cloud at a trapping power of 1.1 W (see Fig. 1). The total atom number and temperature is extracted from this in-situ image: typical values are around $3 \cdot 10^6$ atoms at 1 µK giving a reference phase space density $\mathrm{PSD}_o \approx 0.25$. The influence of this pulse is at the 1% level in terms of heating and even lower in terms of atom losses. This minimally destructive probing was chosen to allow for the exploration of the maximal possible range of condensate fractions.

Thus, a reference PSD is known for each run of the experiment before the phase transition occurs. Assuming that the subsequent evaporation efficiency is deterministic, the critical dipole trap power, P_c, at which the phase transition is crossed can be predicted. A high PSD_o will lead to efficient evaporation and thereby a phase transition at high optical power. If PSD_o is reduced, P_c reduces until a BEC is no longer obtained below a certain PSD_o. The dependence of P_c on PSD_o defines a *critical curve* illustrated in the inset of Fig. 1(b). In the following we use this example to demonstrate the benefits of dispersive probing for the determination of phase diagrams in the presence of environmentally induced fluctuations.

In the absence of the DB probe, PSD_o is not known in a particular realization. The critical curve can, however, be determined approximately by assuming slowly varying experimental conditions and repeatedly interchanging two sequences of measurements: one in which the evaporation sequence was interrupted early to determine PSD_o and one with the normal evaporative cooling sequence to BEC. The fact that the particular PSD_o is not known for the latter sequence introduces fundamental limitations for obtaining low error bars by averaging over several realizations as shown below.

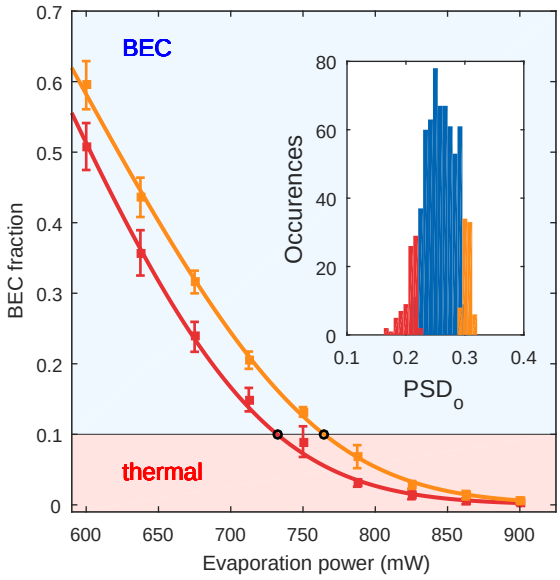

Figure 2. (Color online) BEC growth curves from absorption imaging data for different PSD bins. The inset shows the corresponding histogram of PSDs round 1.1 W. The red and yellow shaded areas depict the two selected data groups for the respective growth curves.

In a first set of experiments, absorption images were acquired at 9 different points during the last linear evaporation ramp between 900 and 600 mW. The predictive power of our DB method is quantified by binning different experimental runs in which PSD_o is approximately equal. The critical power in each bin is then determined by fitting the condensate fraction with the heuristically motivated function $N_0/N = \alpha(P-\beta)/[1-\exp(\gamma(P-\beta))]$ where P denotes the dipole beam powers at which the cloud is released for absorption imaging, P_{off} is related to the transition point, and α, β and γ are fitting parameters. To limit the systematic error due to inaccurate analysis of absorption images at small condensate fraction, the critical power, P_c, is determined from the point at which the fitted growth function reaches 10 % BEC fraction. For illustration, we first apply this procedure to two groups of data points (see inset of Fig. 2). As expected, a clear systematic shift between the two groups is seen in Fig. 2.

In the following we examine more systematically how much information about the shape of the critical curve can be extracted. For each of the 21 bins, the BEC growth function is obtained and P_c and its standard error are extracted [30] (see Fig. 3).These critical powers are then fitted with a quadratic model [31]. From the confidence bounds (68 %) of the fit, we obtain the standard error on the estimated P_c. Comparing the confidence bounds of the quadratic fit with the result

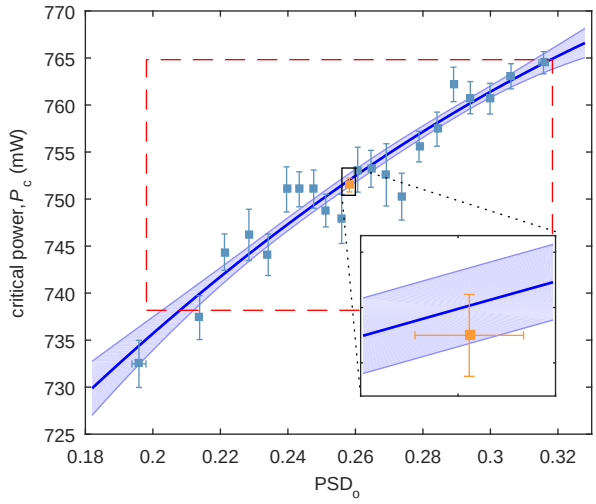

Figure 3. (Color online) Experimental determination of the critical curve corresponding to a section of the inset of Fig. 1(b). Each blue point is obtained from 4 individual evaporation series. The horizontal error bars correspond to the standard error of the PSD in each bin. The yellow point is the result of evaluating the whole data set without binning. The dashed red box is ± 2 standard deviations of the whole dataset and highlights the skewedness of the data. The inset highlights ($\mathrm{PSD}_o = 0.256$–0.26, $P_c = 750.4$–$753.3\,\mathrm{mW}$) the area around the point representing the whole dataset and shows its systematic shift compared to a quadratic fit to the binned data.

of averaging all the data (orange point in the inset of Fig. 3), both methods give similar uncertainties at this particular point. This demonstrates clearly the first main result of this Letter: the DB-method gives a dramatic increase in the obtained information about the critical curve without a noticeable decrease in precision.

Moreover, indiscriminately averaging all data points assumes a linear response over the entire range. This is not valid as shown by the fit. The inset of Fig. 3 demonstrates clearly that the error bounds from simple averaging do not represent the true bounds. This illustrates another key point of this Letter: in the case of even slightly non-linear dependence on the control variable the precision does not improve with averaging of more data samples as is conventionally assumed. On the contrary, it leads to inaccuracy and misleading error bounds.

This effect can be understood based on the following argument, which is valid for any measurement with a noisy control parameter. Assuming a control parameter x that is fluctuating with a variance σ_x^2, the average over many realizations of an experimental outcome following some function $f(x)$ yields a systematically shifted value $\langle f(x)\rangle = f(x) + \frac{1}{2} f''(x)\sigma_x^2$ [30]. In the case of averaging all data this shift is $\Delta = 0.25\,\mathrm{mW}$, while our binning results in a negligible shift of $5.1\,\mu\mathrm{W}$ for the whole curve.

In general, if there is no a priori knowledge of the shape of the critical curve, a conservative estimate would have to employ the standard deviation illustrated by the dashed box in Fig. 3. This highlights the usefulness of the DB-approach for the sensitivity-enhancement of general quantum simulation experiments. In this particular case, the benchmark method yields a prediction precision improvement of a factor of 10 compared to the necessarily conservative estimate. We emphasize the relative simplicity of the technique, which can easily be implemented in existing setups as a post-selection tool or used to study the stochastisticity of quantum phase transition dynamics.

To quantify the predictability in more detail, we compare the variance of absorption measurements in the vicinity of the BEC transition to the conditional variance given the knowledge of the benchmarking probe. Slightly before the transition point, we obtain a reduction in variance by a factor 14, whereas after the transition point the reduction decreases steadily ending at roughly 2 [30]. We attribute this drastic drop to a combination of small classical fluctuations, such as trap bottom instabilities, and quantum noise arising due to the stochastic nature of the condensation process [32]. The drop demonstrates that single benchmark measurements cannot give detailed information on the stochastic dynamics in the region around the quantum phase transition.

We therefore turn to a natural extension of this approach; repeated probing of the crossing of the phase transition in a single realization. We discuss two cases: first repeated probing of evaporative cooling and second probing of multiple consecutive conservative phase transition crossings.

Based on a detailed understanding of the individual in-situ images [30], we repeatedly probe the sample in a single evaporative run. The ultimate goal is accurate probing of the transition at the quantum limit. This is at present limited by classical fluctuations in the probing light and the trap geometry as well as insufficient imaging resolution, which will be topics of future research. Here we address an important first step: the modification of the phase transition due to the heating caused by the probing. This is important for all future studies due to the intrinsic trade-off between destructivity and signal to noise in dispersive probing.

During the final stages of the evaporation process up to 6 pulses are taken at 220 ms intervals for various pulse durations. After the final pulse in the sequence an absorption image is taken and the condensed fraction extracted. The results of this in-situ probing of the condensation process using three different probe durations are shown in Fig. 4(a). A clear shift of the BEC transition point towards lower dipole powers and shallower traps is observed for increasing pulse durations due to heating. The red curve in Fig. 4(a) demonstrates the systematic shift introduced by the Faraday probing which is confirmed by absorption images at the end of the sequence [30]. The observed heating rate is somewhat higher than simple theoretical estimates would suggest, which we attribute both to classical variations in probing conditions and to multiple scattering events due to the high spatial density. Our results reinforce the need to consider heating effects in future studies of the quantum effects of dispersive probing [28, 29].

Finally, we show that the entire BEC phase transition dia-

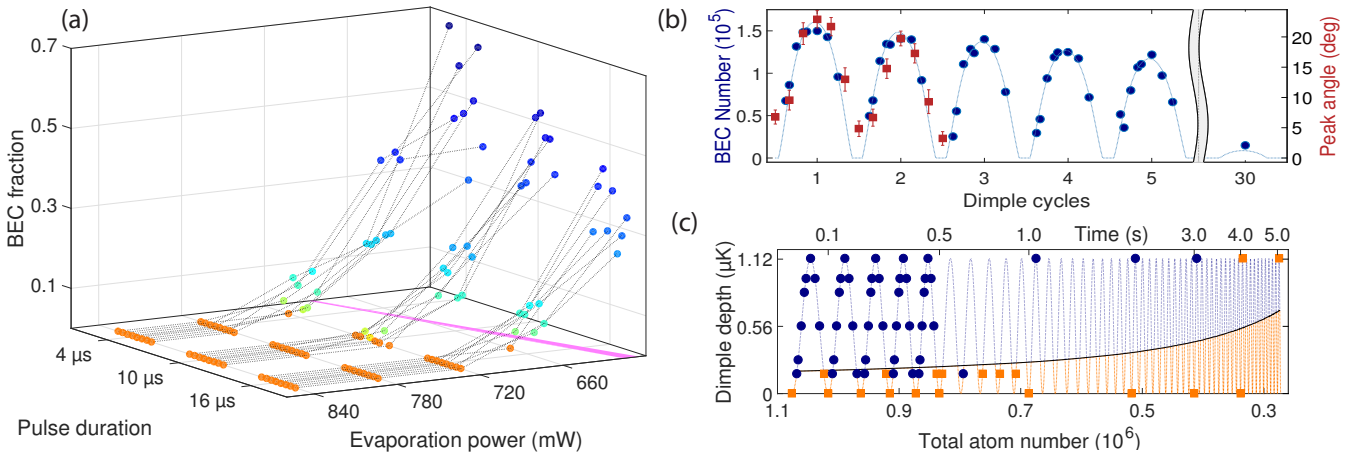

Figure 4. (Color online) (a) Single-shot probing of the BEC formation: For each of the three pulse durations 8 repetitions are shown. The pink line, derived from absorption images, indicates where 10% BEC fraction is crossed (thickness indicates 2σ of confidence bounds). (b) BEC atoms measured via absorption imaging (blue circles) as the dimple trap depth was cycled. Red squares show the peak rotation angle from multiple dispersive images of 2 μs duration during the first two cycles; error bars correspond to 1σ over several repetitions. (c) Phase-diagram of the atoms in the dimple potential. Above the black line a BEC should be observed (blue part of the sinusoidally cycling curve), while below one expects only thermal atoms (orange part). The blue dots indicate absorption measurements containing a BEC, while the orange squares indicate purely thermal clouds.

gram can be mapped in a single-run using the periodic addition of a focused "dimple" potential [33]. The dimple allows for the repeated conservative crossing between thermal cloud and BEC. Studies to date have only employed this effect in combination with individual, destructive absorption images: BEC production has been characterized [34–36] and in one pioneering experiment multiple crossings explored [37]. In our experiments the evaporation is stopped before condensation is reached. At this point the cloud serves as a reservoir in which a 912 nm wavelength laser beam focused to a waist of 7 µm produces an additional potential. In our experiments this potential is periodically cycled from a depth of 0 to 1.12 µK .

We first characterize the cloud evolution with absorption imaging. Maximum BEC atom numbers of around $1.5{\cdot}10^5$ atoms, 10% of the total atom number, are measured while after 30 cycles the condensed cloud of $2{\cdot}10^4$ atoms is still distinguishable from the thermal reservoir, see Fig. 4(b). The total atom number decay and the reservoir temperature increase are used to estimate a critical dimple depth. Thus, we can place the experimental results into two groups on a phase diagram, see Fig. 4(c). The condensation dynamics in the dimple involves three parts of the sample (reservoir, BEC and thermal fractions in the dimple). We find that even a simple model [30] can predict the presence/absence of a BEC reasonably well during the first 20 cycles. Inaccuracy in the measurement of the reservoir temperature and non-adiabatic dimple loading dynamics reduce the effectiveness of the model to make predictions on the final cycles.

Next, we perform the first dispersive probing of multiple quantum phase transitions by introducing a varying number of weak Faraday pulses within each dimple cycle at different pulse durations. In Fig. 4(b) red squares indicate the maximal angle of Faraday rotation obtained in each probing pulse. The non-zero signal in the absence of the dimple is caused by the background polarisation rotation of the reservoir. The data clearly demonstrate our ability to track the loading into the dimple over two realizations of the BEC production [38]. Finally, we study the destructivity of the probing by interrupting the probing at various points and determine the number of condensed atoms using absorption imaging. For a single weak probe applied repeatedly at maximum dimple power at least 10 dimple cycles can be monitored whereas only a few transitions can be monitored when seven pulses per cycle are applied [30]. This means that both correlation measurements between, as well as high-resolution monitoring of, several quantum phase transitions in a single shot should be feasible.

In summary, we have demonstrated the predictive power of non-destructively probing a cold cloud before it crosses the BEC phase transition. This provides enhanced information about the non-linear dependence of a phase transition on a control parameter. Importantly we demonstrate that using conventional methods the precision of a quantum simulation does not necessarily increase with additional repetitions unlike our method. We envision similar techniques to be applicable for any quantum many-body phase transition in which classical fluctuations play a role. In addition, we have demonstrated repeated probing of both one and several phase transitions in a single shot. This enables the single-realization mapping of full phase diagrams as well as the investigation of stochastic effects such as increased fluctuations at the phase transition [32] and possible non-Markovian dynamics [39] for multiple crossings.

ACKNOWLEDGMENTS

The authors acknowledge fruitful discussions with E. Zeuthen, J. H. Müller and K. Mølmer. This work was supported by the Danish Council for Independent Research, the Lundbeck Foundation, the Villum Foundation, the European Research Council, and Marie Curie IEF.

---

* M. G. Bason and R. Heck contributed equally to this work

† Electronic address: sherson@phys.au.dk

[1] I. Georgescu, S. Ashhab, and F. Nori, Rev. Mod. Phys. **86**, 153 (2014).

[2] I. Bloch, J. Dalibard, and S. Nascimbène, Nat. Phys. **8**, 267 (2012).

[3] J. Dalibard, F. Gerbier, G. Juzelinas, and P. Öhberg, Rev. Mod. Phys. **83**, 1523 (2011).

[4] J. Simon, W. S. Bakr, R. Ma, M. E. Tai, P. M. Preiss, and M. Greiner, Nature **472**, 307 (2011).

[5] J. Struck, C. Ölschläger, R. Le Targat, P. Soltan-Panahi, A. Eckardt, M. Lewenstein, P. Windpassinger, and K. Sengstock, Science **333**, 996 (2011).

[6] J. W. Britton, B. C. Sawyer, A. C. Keith, C.-C. J. Wang, J. K. Freericks, H. Uys, M. J. Biercuk, and J. J. Bollinger, Nature **484**, 489 (2012).

[7] A. A. Houck, H. E. Türeci, and J. Koch, Nat. Phys. **8**, 292 (2012).

[8] A. Aspuru-Guzik and P. Walther, Nat. Phys. **8**, 285 (2012).

[9] S. Trotzky, L. Pollet, F. Gerbier, U. Schnorrberger, I. Bloch, N. V. Prokof'ev, B. Svistunov, and M. Troyer, Nat. Phys. **6**, 998 (2010).

[10] M. R. Andrews, M.-O. Mewes, N. J. van Druten, D. S. Durfee, D. M. Kurn, and W. Ketterle, Science **273**, 84 (1996).

[11] C. C. Bradley, C. A. Sackett, and R. G. Hulet, Phys. Rev. Lett. **78**, 985 (1997).

[12] H.-J. Miesner, D. M. Stamper-Kurn, M. R. Andrews, D. S. Durfee, S. Inouye, and W. Ketterle, Science **279**, 1005 (1998).

[13] G. Lamporesi, S. Donadello, S. Serafini, F. Dalfovo, and G. Ferrari, Nat. Phys. **9**, 656 (2013).

[14] J. H. V. Nguyen, P. Dyke, D. Luo, B. A. Malomed, and R. G. Hulet, Nat. Phys. **10**, 918 (2014).

[15] B. J. Sawyer, A. B. Deb, T. McKellar, and N. Kjærgaard, Phys. Rev. A **86**, 065401 (2012).

[16] M. Gajdacz, A. J. Hilliard, M. A. Kristensen, P. L. Pedersen, C. Klempt, J. J. Arlt, and J. F. Sherson, "Preparation of ultracold atom clouds at the shot noise level," (2016), arXiv:1604.05087 [quant-ph].

[17] S. S. Szigeti, M. R. Hush, A. R. R. Carvalho, and J. J. Hope, Phys. Rev. A **82**, 043632 (2010).

[18] M. R. Hush, S. S. Szigeti, A. R. R. Carvalho, and J. J. Hope, New J. Phys. **15**, 113060 (2013).

[19] A. C. J. Wade, J. F. Sherson, and K. Mølmer, Phys. Rev. Lett. **115**, 060401 (2015), arXiv:1504.04241v1.

[20] K. Eckert, Ł. Zawitkowski, A. Sanpera, M. Lewenstein, and E. S. Polzik, Phys. Rev. Lett. **98**, 100404 (2007).

[21] B. Rogers, M. Paternostro, J. F. Sherson, and G. De Chiara, Phys. Rev. A **90**, 043618 (2014).

[22] M. K. Pedersen, J. J. W. H. Sørensen, M. C. Tichy, and J. F. Sherson, New J. Phys. **6**, 113038 (2014).

[23] G. Mazzucchi, W. Kozlowski, S. F. Caballero-Benitez, T. J. Elliott, and I. B. Mekhov, Phys. Rev. A **93**, 023632 (2016), arXiv:1503.08710.

[24] P. Hauke, R. J. Sewell, M. W. Mitchell, and M. Lewenstein, Phys. Rev. A **87**, 021601 (2013).

[25] J. E. Lye, J. J. Hope, and J. D. Close, Phys. Rev. A **67**, 43609 (2003), arXiv:0302568 [cond-mat].

[5] M. Gajdacz, P. L. Pedersen, T. Mørch, A. J. Hilliard, J. Arlt, and J. F. Sherson, Rev. Sci. Inst. **84**, 083105 (2013), arXiv:1301.3018.

[27] E. O. Ilo-Okeke and T. Byrnes, Phys. Rev. Lett. **112**, 233602 (2014).

[28] P. Bons, R. de Haas, D. de Jong, A. Groot, and P. van der Straten, Phys. Rev. Lett. **116**, 173602 (2016).

[29] P. Wigley, P. Everitt, K. Hardman, M. Sooriyabandara, M. Perumbil, J. Close, N. Robins, and C. Kuhn, "Minimally-destructive Partial Phase Contrast Imaging," (2016), arXiv:1601.04425.

[30] See Supplementary Material.

[31] Since the variation in PSD_o is primarily due to fluctuations in atom number, rather than temperature, the finite curvature is due to the decrease in evaporation efficiency for samples with few atoms and thus a slower collision and re-thermalization rate.

[32] V. V. Kocharovsky and V. V. Kocharovsky, Phys. Lett. A **379**, 466 (2015).

[33] P. W. H. Pinkse, A. Mosk, M. Weidemüller, M. W. Reynolds, T. W. Hijmans, and J. T. M. Walraven, Phys. Rev. Lett. **78**, 990 (1997).

[34] D. Comparat, A. Fioretti, G. Stern, E. Dimova, B. L. Tolra, and P. Pillet, Phys. Rev. A **73**, 043410 (2006).

[35] M. C. Garrett, A. Ratnapala, E. D. van Ooijen, C. J. Vale, K. Weegink, S. K. Schnelle, O. Vainio, N. R. Heckenberg, H. Rubinsztein-Dunlop, and M. J. Davis, Phys. Rev. A **83**, 013630 (2011).

[36] S. Dutta and E. J. Mueller, Phys. Rev. A **91**, 013601 (2015).

[37] D. M. Stamper-Kurn, H.-J. Miesner, A. P. Chikkatur, S. Inouye, J. Stenger, and W. Ketterle, Phys. Rev. Lett. **81**, 2194 (1998).

[38] At present, imaging resolution does not allow to distinguish BEC and thermal parts in the dimple, however experimental reconstruction is currently underway to allow for this in the near future.

[39] Á. Rivas, S. F. Huelga, and M. B. Plenio, Reports Prog. Phys. **77**, 094001 (2014).

Supplementary Material: Measurement-enhanced determination of BEC phase diagrams

MODELLING AND DATA EVALUATION OF SINGLE FARADAY IMAGES

Description of the semi-ideal model

In contrast to time-of-flight absorption imaging where densities are low and the mean-field interaction between the atoms is negligible, the interaction's influence on the cloud's density profile has to be taken into account in the case of in-trap images. Instead of taking the complete influence of mean-field interactions on the condensed and thermal part in a self-consistent way into account, we employ the so-called 'semi-ideal' model [S1–S4], which only includes the interactions of the condensed part on the thermal part which leads to a modified effective trapping potential for the thermal part:

$$V_{\mathrm{eff}}(\mathbf{r}) = V_{\mathrm{ext}}(\mathbf{r}) + 2gn_0(\mathbf{r}). \tag{S1}$$

In the Thomas-Fermi approximation, the condensed and thermal cloud's density distributions are then given by

$$n_0(\mathbf{r}) = \frac{1}{g}\left(\mu - V_{\mathrm{ext}}(\mathbf{r})\right) \quad \text{and} \tag{S2}$$

$$n_{\mathrm{th}}(\mathbf{r}) = \frac{1}{\lambda_{\mathrm{T}}^3} g_{3/2}\left(e^{\beta(\mu - V_{\mathrm{eff}}(\mathbf{r}))}\right). \tag{S3}$$

where λ_{T} is the thermal de-Broglie wavelength. Usually, the chemical potential μ and the number of condensed atoms N_0 have to be determined self-consistently. We circumvent this by applying a further simplification and expanding the condensed fraction into a series depending on the reduced chemical potential $\bar{\mu} = \frac{\mu}{k_B T}$ [S2]. Truncation after the first non-trivial order and solving for the condensate fraction yields:

$$\frac{N_0}{N} = 1 - \left(\frac{T}{T_c}\right)^3 - \eta\frac{\zeta(2)}{\zeta(3)}\left(\frac{T}{T_c}\right)^2\left[1 - \left(\frac{T}{T_c}\right)^3\right]^{2/5}, \tag{S4}$$

η is a dimensionless scaling parameter described by $\eta = \frac{\mu_{T=0}}{k_B T}$ and T_c the critical temperature for the onset of condensation for a non-interacting, ideal gas $k_B T_c = \frac{\hbar\bar{\omega}N^{1/3}}{\zeta(3)^{1/3}}$, with the Riemann zeta function ζ.

Given a cloud with atom number N at temperature T, we are now able to calculate the expected condensate fraction and the density distributions for thermal and condensed part, respectively.

Fitting technique

To extract information about atom number, temperature and BEC fraction from the in-situ Faraday probe, each image is first converted from EMCCD counts into a rotation angle. Given atoms in the same internal state with z axis angular momentum projection $\langle \hat{f}_z \rangle$ the spatially dependent Faraday rotation is [S5]:

$$\theta_{\mathrm{F}} = \frac{\langle \hat{f}_z \rangle \Gamma \lambda^2}{16\pi\Delta} \int n(\mathbf{r}) dz, \tag{S5}$$

where Γ is the excited state lifetime, λ the imaging light wavelength, Δ the excited state detuning and $n(\mathbf{r})$ is the density distribution.

The resulting image is azimuthally averaged around the point with the highest rotation angle (see Fig. S1). This radial profile is then compared to multiple profiles obtained for realizations of the 'semi-ideal model' with atom clouds of different N and T and a given trap geometry. The best agreeing pair of N and T is found. The obtained peak densities are within 20% of those extracted from absorption images.

A problem arises for clouds which are just above the condensation threshold. Note that due to interactions this corresponds to temperatures $T < T_c$. Hence, there is a range of temperatures, where a BEC is predicted for a non-interacting gas, but not according to our implementation of the semi-ideal model. In order to close this gap, we linearly interpolate the

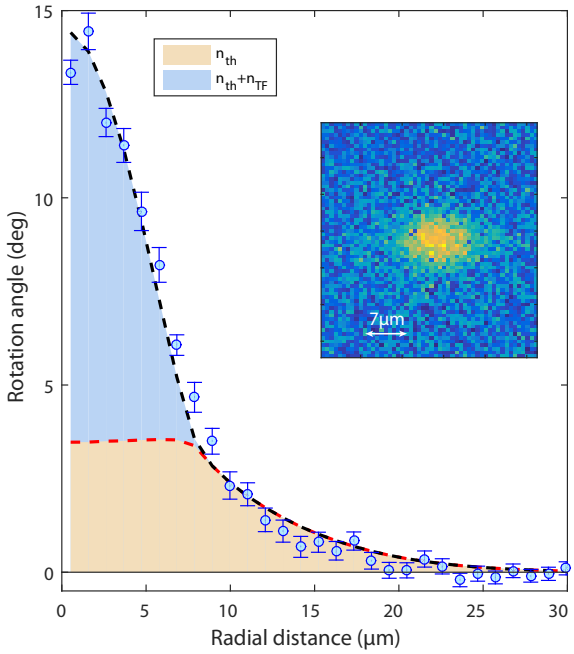

Figure S1. (Color online) Azimuthal averaging and fitting with the semi-ideal model. The raw image (shown in the inset) is azimuthally averaged around the point with the highest rotation angle (blue data points, the errorbars depict the standard deviation obtained in the averaging process). The averaged data is compared to different results of calculations for the semi-ideal model and the best agreement is found. The red dashed line shows the thermal atom distribution of the best fitting realization, the blue dashed line the corresponding sum of thermal and condensed atom distribution.

density distributions between the cases of just having a small interacting BEC and a non-interacting thermal cloud in this temperature range.

ACCURACY OF FARADAY IMAGES

The BEC fraction extracted in-situ (as described above) is directly compared to the fraction measured from absorption imaging. For this comparison, we use a single non-destructive pulse of varying duration. A range of potential depths across the BEC transition are chosen and the cloud profiles recorded. BEC fractions from the fitted profiles are then compared to those measured for the same potential with absorption imaging. This analysis (see fig. S2(a)) shows a systematic shift towards higher BEC fractions in the in-situ images and best agreement for long durations.

To understand the origin of this trend we model the effect of finite photon numbers on the determination of BEC fractions. For a given photon flux and cloud profile we generate sample images which include the Poissonian statistics of the imaging light and apply the fitting procedure described previously. The mean and standard deviation in BEC fraction are then extracted from the series of images and repeated for different photon fluxes. The results shown in figure S2(b) demonstrate a clear, systematic shift consistent with observations. This effect persists for all the three simulated condensate fractions. The range of photon fluxes used in the experiment (yellow bar) indicate that agreement between in-situ and absorption imaging cannot be expected for higher condensate fractions. We attribute this effect to a low signal-to-noise level in the thermal wings of the cloud such that parts are below the detection limit. Therefore, the clouds appear to be purer in terms of condensate fraction.

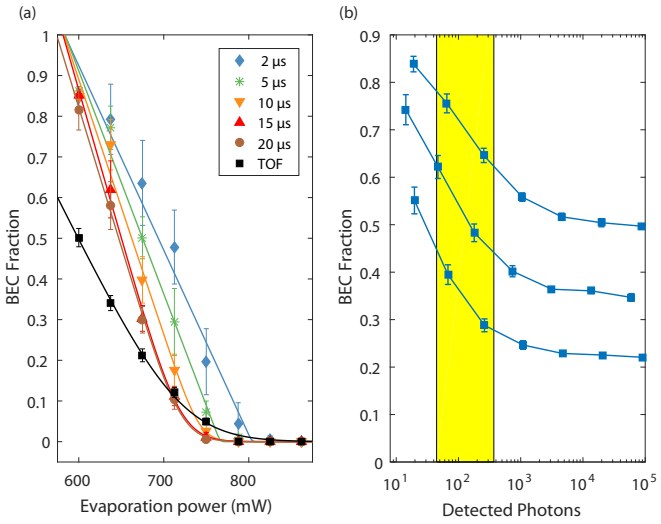

Figure S2. (Color online) (a) Single Faraday probing of the BEC transition for different imaging pulse durations (colored symbols) compared to results of conventional absorption imaging (black squares). The systematic overestimation of BEC fractions obtained in Faraday imaging is visible. (b) Simulation of the influence of shot noise on the fit results in Faraday imaging as a function of mean number of detected photons. For the modelling, realistic pairs of total atom number N and temperature T were chosen corresponding to three different BEC fractions (from top to bottom $\frac{N_0}{N} = 0.50$, 0.35 and 0.23). The lines are guides to the eyes. A clear systematic shift of the BEC fraction is observed for photon numbers below 10^3. The yellow bar indicates the photon numbers used in our experiments.

CORRELATIONS BETWEEN DISPERSIVE BENCHMARK AND ABSORPTION IMAGING

Given the predictive power of the benchmarking technique demonstrated in the main text, it is interesting to explore the limits of this approach. This is achieved by evaluating the correlations between the benchmark pulse and absorption measurements taken at various final trap depths. A measurement of peak angle during a benchmark pulse and the total atom number inferred from absorption imaging is show in figure S3(a). We define the noise reduction factor (NRF) for the variables x, y as the ratio between the original and reduced variances:

$$NRF = \frac{\sigma_y^2}{\sigma_{y,red}^2}, \tag{S6}$$

$$\sigma_{y,red}^2 = \frac{1}{N-1}\sum_{i=1}^{N}\left[y_i - \bar{y}(x_i)\right]^2, \tag{S7}$$

where $\bar{y}(x)$ is determined by simple linear regression. Stronger correlations result in higher values of NRF.

The associated NRFs are shown in figure S3(b). Well before the transition there is a strong correlation between the two variables which quickly decays following the onset of condensation. The total atom number NRF is higher than 10 for points close to the BEC transition and decreases significantly to almost 2 for the data points at the lowest final evaporation power, 600 mW. This drastic drop in predictability is attributed to a combination of small classical fluctuations of the trap bottom and quantum noise arising due to the stochastic nature of the condensate formation.

SYSTEMATIC SHIFT OF EXPERIMENTAL OUTCOMES

As described in the main letter, experimental outcomes are subject to systematic shifts as soon as the control variable fluctuates and the system shows a non-linear response. This effect can be understood and quantified by the following argument, which is valid for any measurement with a controlled but fluctuating variable. Assuming a control variable x that fluctuates around its mean by some amount x', each realization of an experimental outcome following some function $f(x)$ will be measured at slightly different values $x = \langle x \rangle \pm x'$. The mean

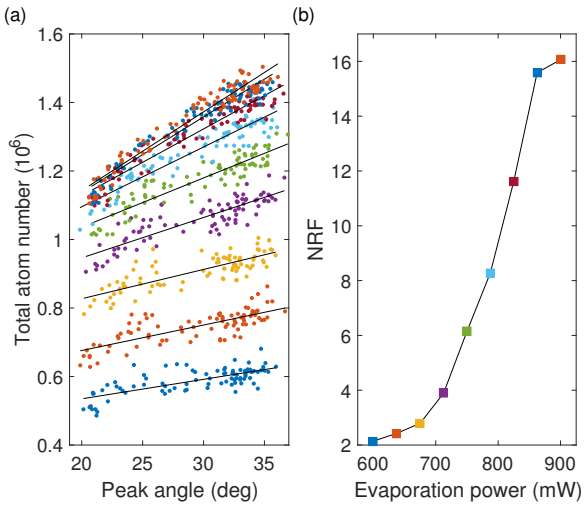

Figure S3. (Color online) (a) Correlation plots between the peak rotation angle from the dispersive benchmark probing and the total atom number from absorption imaging for various final trap depths (from top to bottom: higher to lower final evaporation power). (b) The extracted NRFs are shown for the different final evaporation powers.

measurement result $f_{\mathrm{meas}} = \langle f(x) \rangle$ will simply be the convolution of the true response function with the distribution of the control variable. In the case of a normally distributed fluctuating control variable with variance σ_x^2 and assuming that the fluctuations are sufficiently small such that $f(x)$ can be approximated by its Taylor expansion to second order, one finds a relatively simple differential equation showing the introduced systematic shift, $f_{\mathrm{meas}} = f(x) + \frac{1}{2} f''(x) \sigma_x^2$. A more general calculation leads to the same result even for non-Gaussian distributions of control values [S6]. Since we assume a quadratic fit to our measured data the offset to the "true" result can easily be found. The whole curve is shifted by $\Delta = -1/2 f''_{\mathrm{meas}} \sigma_x^2$.

TOF ANALYSIS OF MULTIPLE PROBING EXPERIMENTS

In the main text we present the repeated probing of the sample in a single evaporative run. The in-situ data show a shift in the determined BEC transition point due to heating by the same probing pulses. Here we discuss how this shift is confirmed by absorption images in TOF taken after the final Faraday probing pulse in the sequence. The results of this analysis are shown as the pink line in Fig. 4(a) (main text).

The extracted BEC fractions are shown in Fig. S4. The data corresponding to the same Faraday probing pulse duration are fitted with the heuristically motivated function $N/N_0 = \alpha(P-\beta)/[1-\exp(\gamma(P-\beta))]$, described in the main text. Note that even with the high signal-to-noise of absorption imaging there are still difficulties associated with correctly measuring small BEC fractions. This is illustrated by the fact that the dataset corresponding to the highest probe duration is not pulled as much towards zero around the transition as

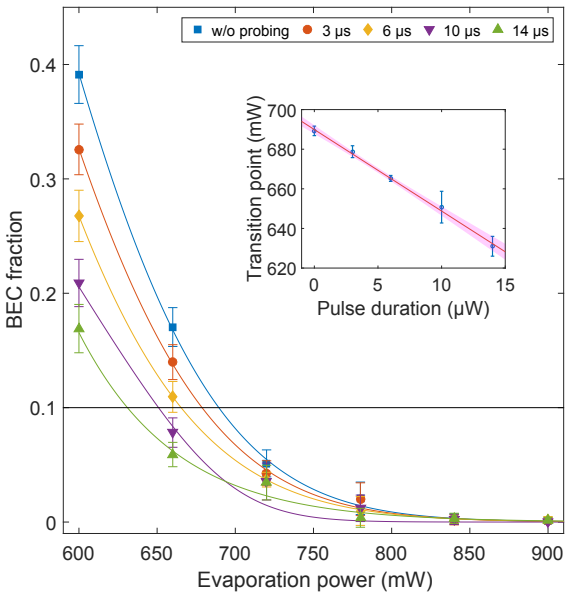

Figure S4. (Color online) BEC fraction measured via absorption imaging after multiple pulses of Faraday probing have interacted with the sample. Data and corresponding fits are shown for different durations. In the inset the 10% transition point is plotted vs. the Faraday pulse duration. The shaded pink area is from the 2σ confidence bounds of a linear regression.

the other series. For this reason we define the transition point as the level of evaporation power where the fitted BEC fraction reaches 10%, and define its error from the 1σ confidence bounds. The resulting BEC transition points together with the corresponding pulse durations are fitted with a linear function. This fit function and its 2σ confidence bounds are reported in Fig. 4(a) (main text).

DIMPLE PHASE-DIAGRAM

In this section we describe the procedure to model the repeated crossing of the BEC phase transition, achieved via a periodically modulated 'dimple' potential at a rate of 10 Hz.

After a variable number of full dimple cycles, we measure the conditions of the cloud that serves as a reservoir with absorption imaging in TOF. The extracted number of atoms and temperature are shown in Fig. S5. The atom number is well fitted by a double exponential function: the initial decay corresponds to a lifetime of about 0.2 s and is followed by a slower decay with a lifetime of about 1.5 s.

The temperature data are fitted with a linear function, resulting in an initial temperature of $0.37(1)$ µK and a heating rate of $9(5)$ nK/s. The uncertainties on the fit results are although quite broad, due to difficulties in measuring temperatures accurately on clouds very close to the BEC transition.

From the temperature and the trapping frequencies, the rms

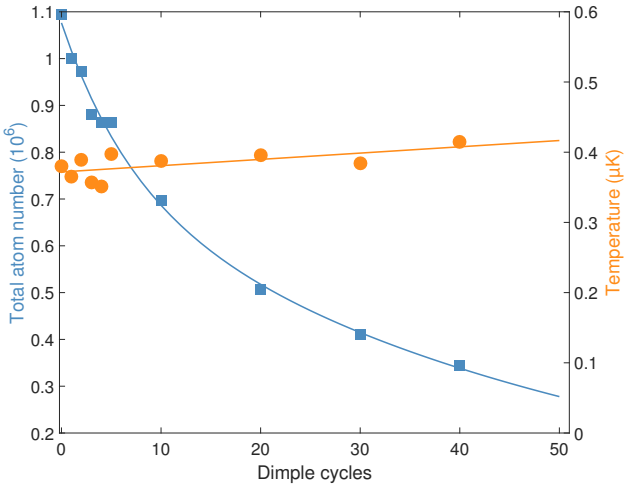

Figure S5. (Color online) Reservoir atom number (blue squares) and its temperature (orange dots) as measured with absorption imaging at the beginning of the corresponding dimple cycle. The curves are fits to the data: double exponential for the atom number and linear for the temperature.

radius of the reservoir cloud is calculated to be between 13 and 19 μm. On the contrary, the dimple beam has a waist of only 7 μm. Because of the different sizes we can distinguish the increase in density due to the atoms trapped in the dimple potential using in-situ dispersive Faraday probing. In this way, we can estimate that 50 % of the reservoir atoms concentrate in the volume defined by the dimple, when this is at its deepest value of 1.12 μK. We use only this portion of the atoms in the following calculations.

From the fitted atom number and the time-varying trapping frequencies of the cycling dimple potential we calculate the critical temperature for the non-interacting gas, T_c (see section), as a function of time; we compare this with the fitted temperature. When interaction is included, equation (S4) gives non-zero condensate fractions when $T/T_c < 0.88$ for our experimental conditions.

These calculations are visualised in a phase-space diagram, Fig. 4(c) (main text), where the total atom number and the depth of the dimple are the set of independent variables. The cycling dimple potential draws a line, which crosses the critical boundary corresponding to the threshold value for T/T_c. The experimental data was arranged on the diagram accordingly.

* M. G. Bason and R. Heck contributed equally to this work
† Electronic address: sherson@phys.au.dk

[S1] A. Minguzzi, S. Cont, and M. P. Tosi, J. Phys. Condens. Matter **9**, L33 (1997), arXiv:9612190 [cond-mat].

[S2] M. Naraschewski and D. M. Stamper-Kurn, Phys. Rev. A **58**, 2423 (1998), arXiv:9803216v1 [arXiv:cond-mat].

[S3] F. Gerbier, J. H. Thywissen, S. Richard, M. Hugbart, P. Bouyer, and A. Aspect, Phys. Rev. A **70**, 1 (2004), arXiv:0401585 [cond-mat].

[S4] R. Meppelink, R. A. Rozendaal, S. B. Koller, J. M. Vogels, and P. van der Straten, Phys. Rev. A **81**, 053632 (2010).

[S5] M. Gajdacz, P. L. Pedersen, T. Mørch, A. J. Hilliard, J. Arlt, and J. F. Sherson, Rev. Sci. Inst. **84**, 083105 (2013), arXiv:1301.3018.

[S6] K. Mølmer, private communication.